Carbenium ion-mediated oligomerization of methylglyoxal for secondary organic aerosol formation

Yuemeng Ji[a,b,c,d,1], Qiuju Shi[a,b], Yixin Li[c,d,1], Taicheng An[a,b,2], Jun Zheng[e], Jianfei Peng[c,d], Yanpeng Gao[a,b], Jiangyao Chen[a,b], Guiying Li[a,b], Yuan Wang[f], Fang Zhang[c,d,g], Annie L. Zhang[h], Jiayun Zhao[c,d], Mario J. Molina[i,2], and Renyi Zhang[c,d,2]

[a]Guangdong Key Laboratory of Environmental Catalysis and Health Risk Control, Institute of Environmental Health and Pollution Control, Guangdong University of Technology, Guangzhou 510006, China; [b]Guangzhou Key Laboratory Environmental Catalysis and Pollution Control, School of Environmental Science and Engineering, Guangdong University of Technology, Guangzhou 510006, China; [c]Department of Atmospheric Sciences, Texas A&M University, College Station, TX 77843; [d]Department of Chemistry, Texas A&M University, College Station, TX 77843; [e]Collaborative Innovation Center of Atmospheric Environment and Equipment Technology, Nanjing University of Information Science and Technology, Nanjing 210044, China; [f]Division of Geological and Planetary Sciences, California Institute of Technology, Pasadena, CA 91125; [g]State Key Laboratory of Earth Surface Processes and Resource Ecology, College of Global Change and Earth System Science, Beijing Normal University, Beijing 100875, China; [h]Department of Chemistry, College of Natural Sciences, The University of Texas at Austin, Austin, TX 78712; and [i]Department of Chemistry and Biochemistry, University of California San Diego, La Jolla, CA 92093

Contributed by Mario J. Molina, April 10, 2020 (sent for review July 16, 2019; reviewed by Yiqin Gao and Keith Kuwata)

Secondary organic aerosol (SOA) represents a major constituent of tropospheric fine particulate matter, with profound implications for human health and climate. However, the chemical mechanisms leading to SOA formation remain uncertain, and atmospheric models consistently underpredict the global SOA budget. Small α-dicarbonyls, such as methylglyoxal, are ubiquitous in the atmosphere because of their significant production from photooxidation of aromatic hydrocarbons from traffic and industrial sources as well as from biogenic isoprene. Current experimental and theoretical results on the roles of methylglyoxal in SOA formation are conflicting. Using quantum chemical calculations, we show cationic oligomerization of methylglyoxal in aqueous media. Initial protonation and hydration of methylglyoxal lead to formation of diols/tetrol, and subsequent protonation and dehydration of diols/tetrol yield carbenium ions, which represent the key intermediates for formation and propagation of oligomerization. On the other hand, our results reveal that the previously proposed oligomerization via hydration for methylglyoxal is kinetically and thermodynamically implausible. The carbenium ion-mediated mechanism occurs barrierlessly on weakly acidic aerosols and cloud/fog droplets and likely provides a key pathway for SOA formation from biogenic and anthropogenic emissions.

secondary organic aerosol | aqueous | oligomerization | brown carbon | cationic

Fine particulate matter (PM) has been unequivocally associated with adverse effects on human health, representing one of the greatest public epidemics (1–4). Exposure to fine PM has been identified as the cause of more than 7 million premature deaths a year worldwide (4). In addition, fine aerosols exert profound impacts on cloud formation, weather, and climate (5). In the troposphere, secondary organic aerosol (SOA) constitutes a major component of the global fine PM (typically the largest mass fraction) and is produced from photochemical oxidation of biogenic and anthropogenic volatile organic compounds (VOCs) (1, 6). Photochemical oxidation of VOCs yields various products, some of which engage in aerosol nucleation and growth by condensation, gas/particle partitioning, and heterogeneous reactions (1, 6, 7). However, the global SOA budget is consistently underpredicted in atmospheric models (8), and there is growing recognition of the important role of aqueous chemistry in the SOA growth (1, 9, 10). In particular, the SOA formation mechanism likely regulates the aerosol direct and indirect radiative forcing, which has been identified as the largest uncertainty in climate predictions (5, 11, 12).

Small α-dicarbonyls of glyoxal and methylglyoxal (MG) are ubiquitous in the atmosphere (1, 13). Specifically, the oxidation of aromatics (toluene, xylenes, or trimethylbenzenes) and diketones from traffic and industrial sources and biogenic isoprene leads to significant production of MG on urban, regional, and global scales (1, 6, 7, 14). A modeling study predicted the global sources of 45 $Tg{\cdot}a^{-1}$ for glyoxal and 140 $Tg{\cdot}a^{-1}$ for MG, with an estimated global SOA production of 11 $Tg{\cdot}C{\cdot}a^{-1}$ from both species (13). MG oligomers were identified as the major SOA components from aromatic photochemical oxidation in an environmental chamber study (15). Also, reactive and irreversible uptakes of glyoxal and MG were observed on dilute bulk sulfuric acid solution (16, 17). On the other hand, several experimental studies showed that submicrometer ammonium sulfate/sulfuric acid particles exhibited negligible growth upon exposure to high levels of gaseous MG (18–20), but rapid brown carbon (BrC) formation was detected on ammonium/amine-containing particles by reactive MG uptake (19, 21). Currently, the chemical mechanisms for oligomer and BrC formation from small α-dicarbonyls are highly uncertain.

Significance

Secondary organic aerosol (SOA) from photochemical oxidation of volatile organic compounds represents one of the most dominant constituents of fine particulate matter in the troposphere, with profound implications for air quality and climate. However, the fundamental chemical mechanisms leading to SOA formation remain highly uncertain. Here, we show oligomer formation from methylglyoxal with the carbenium ions as the key intermediate using quantum chemical calculations. This cationic oligomerization is demonstrated to proceed via barrierless pathways and occurs at fast rates on weakly acidic aqueous aerosols and/or cloud droplets under typical tropospheric conditions. In contrast to a previously proposed hydration mechanism, out results reveal that the carbenium ion-mediated oligomerization of methylglyoxal provides a major SOA source from anthropogenic and biogenic emissions.

Author contributions: Y.J. and R.Z. designed research; Y.J., Q.S., Y.L., T.A., Y.W., J. Zhao, M.J.M., and R.Z. performed research; Y.J., Y.L., T.A., J. Zheng, J.P., Y.G., J.C., G.L., F.Z., J. Zhao, M.J.M., and R.Z. analyzed data; and Y.J., A.L.Z., and R.Z. wrote the paper.

Reviewers: Y.G., Peking University; and K.K., Macalester College.

The authors declare no competing interest.

[1]Y.J. and Y.L. contributed equally to this work.

[2]To whom correspondence may be addressed. Email: antc99@gdut.edu.cn, mjmolina@ucsd.edu, or renyi-zhang@tamu.edu.

This article contains supporting information online at https://www.pnas.org/lookup/suppl/doi:10.1073/pnas.1912235117/-/DCSupplemental.

First published June 3, 2020.

In this work, we performed theoretical calculations to investigate the aqueous chemistry of MG by considering the solvent effect of water using a continuum solvation model (*Methods*). We established a mechanism of cationic oligomerization for MG and identified the key reaction pathways and intermediates (Fig. 1*A*). The energetics of those pathways were evaluated to assess the feasibility of MG oligomerization leading to atmospheric SOA formation.

Results

We first evaluated the hydration reactions of MG, which was suggested to form diols (DLs), tetrol (TL), and oligomers in aqueous media (16, 22). The activation ($\Delta G^{\ddagger}$) and reaction (ΔG_r) energies depend on H_2O addition to the ketonic or aldehydic group (Fig. 2), each proceeding via a well-defined transition state (TS). The potential energy surface (PES) illustrates that the formation of aldehyde (ADL) and ketone (KDL) diols involves large $\Delta G^{\ddagger}$ (44.1 and 49.4 kcal·mol^{-1}) and small ΔG_r (4.9 and 0.5 kcal·mol^{-1}). The subsequent hydration reactions of ADL and KDL to form TL also occur with large $\Delta G^{\ddagger}$ (38.9 and 41.6 kcal·mol^{-1}) and small ΔG_r (Fig. 3 and *SI Appendix*, Fig. S1). The rate constants (k) of the hydration reactions were determined using the transition state theory (TST), ranging from 10^{-14} to 10^{-22} M^{-1}·s^{-1} (*SI Appendix*, Table S1), indicating that MG hydration is negligible and independent of the concentrations of MG and H_2O. Our calculated $\Delta G^{\ddagger}$ values of MG hydration using the optimized aqueous-phase geometry (see *Methods* and *SI Appendix*, Table S2) are nearly twice larger than those from a previous theoretical study that obtained the solvent energies based on the optimized gas-phase geometry (22).

Next, we explored the cationic oligomerization, including protonation of MG to yield DLs and T**L** and subsequent protonation of DLs and TL to form four first-generation carbenium ions, 1st-CBs (Fig. 1*A*). Each CB engages in association reaction with ADL, KDL, or TL to form the dimers, which then propagate the oligomerization. Protonation of MG is highly exergonic, with the ΔG_r values of −102.4 and −96.1 kcal·mol^{-1} to form two cationic intermediates, CI11 and CI2**1**, respectively (Fig. 2). Alternatively, MG protonation also occurs by the reaction with the hydronium ion (H_3O^+), and the corresponding ΔG_r value of water protonation is −111.0 kcal·mol^{-1}. The negative polarity of the carbonyl O-atom is crucial to provide the characteristic site for protonation. The methyl substituent increases the carbonyl bond polarization, as reflected by a more negatively charged O-atom but a more positively charged C-atom (Fig. 4*A*). As a result, protonation is more favorable at the ketonic group than at the aldehydic group, because of stronger electrostatic attraction. The conversions from CI11 and CI21 to ADL and KDL include sequentially two hydration reactions via additional CIs and a loss of H_3O^+, with the overall ΔG_r values of −3.6 and −14.3 kcal·mol^{-1}, respectively (Fig. 2).

Protonation at the carbonyl site for ADL and KDL to TL forms CI31 and CI41, respectively (Fig. 3 and *SI Appendix*, Fig. S1).

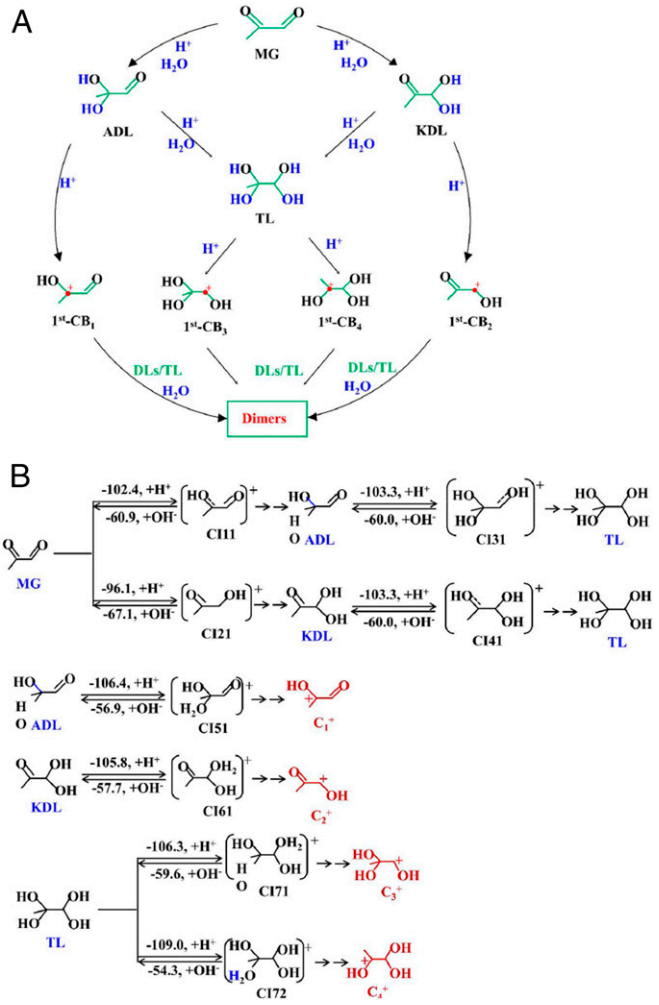

Fig. 1. Reversibility of cationic pathways leading to dimers. (*A*) Starting with MG, the oligomerization mechanism to dimers includes three essential processes, i.e., protonation and hydration to yield DLs and TL, protonation of DLs and TL to form the first-generation carbenium ions (1st-CBs), and association reactions of 1st-CBs with DLs or TL. (*B*) Competing reactions for CIs: reverse reaction with hydroxide ion (OH^-) (denoted by ←) and forward reaction by hydration and protonation to oligomerization (denoted by →). The number denotes the reaction energy (ΔG_r in kilocalories per mole).

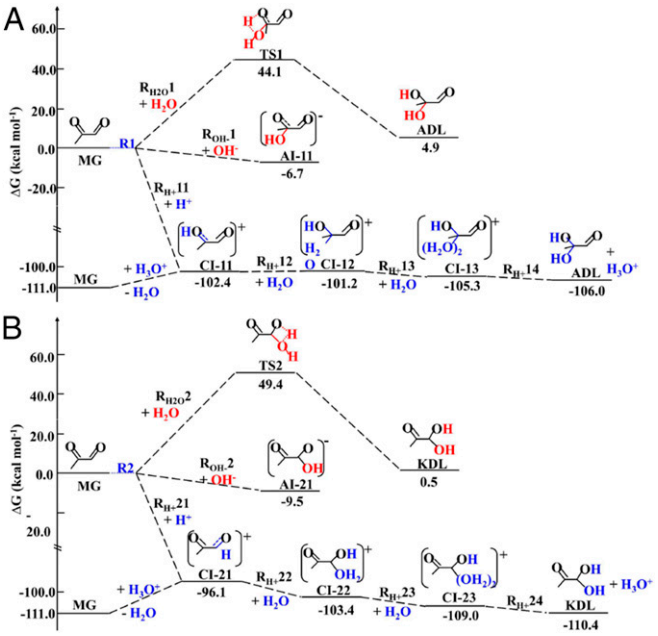

Fig. 2. Competing pathways for diol formation. (*A*) Ketonic pathway from MG to ADL. (*B*) Aldehydic pathway from MG to KDL. From *Left* to *Right*: variations in the PES from MG to ADL and KDL, via direct hydration (*Top*), nucleophilic attack by OH^- (*Middle*), and protonation, hydration, and deprotonation (*Bottom*). The number denotes the activation barrier ($\Delta G^{\ddagger}$) or reaction energy (ΔG_r) for each reaction step.

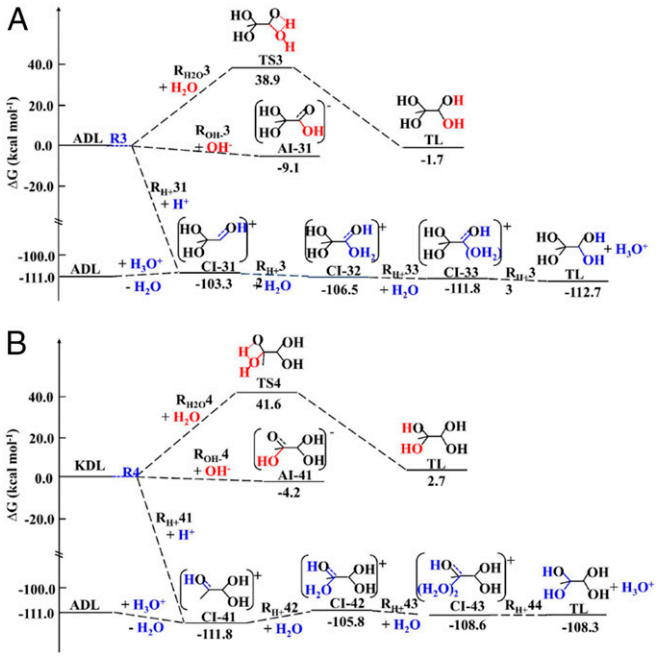

Fig. 3. Competing pathways for tetrol formation. (*A*) Aldehydic pathway from ADL to TL. (*B*) Ketonic pathway from KDL to TL. From *Left* to *Right*: variations in the PES from ADL and KDL to TL, via direct hydration (*Top*), nucleophilic attack by OH^- (*Middle*), and protonation, hydration, and deprotonation (*Bottom*). The number denotes the value of $\Delta G^{\ddagger}$ or ΔG_r for each reaction step, and all energies are relative to MG.

Similarly, CI31 and CI41 can be formed via the hydronium ion pathway. Also, the methyl substituent promotes protonation of KDL (relative to ADL), evident by a larger negative natural charge on the carbonyl O-atom (Fig. 4*A*). For DLs and TL, the O–C bond is elongated because of protonation, and the alcohol O-atom is strongly negatively charged, indicating that both species are liable to nucleophilic addition.

The alternative protonation at the alcohol group for ADL and KDL forms CI51 and CI61, which subsequently undergo dehydration to yield 1st-CB_1 and 1st-CB_2, respectively (*SI Appendix*, Fig. S1*C*). For CI51 and CI61, the O···C distances of the alcohol groups after protonation are elongated to 1.54 and 1.51 Å, respectively, responsible for facile O–C bond cleavage (*SI Appendix*, Fig. S2). Similarly, protonation of TL at the two alcohol groups occurs to form CI71 and CI72 (*SI Appendix*, Fig. S1*C*), which then undergo proton rearrangement and dehydration to form 1st-CB_3 and 1st-CB_4, respectively. Since the O-atom has a larger negative natural charge at the alcohol group than that at the carbonyl site for DLs, the formations of 1st-CB_1 and 1st-CB_2 are more accessible than those of 1st-CB_3 and 1st-CB_4 (or TL). Experimental evidence indicated that DLs are more abundant than TL in aqueous MG solution, with the ratios of 56 to 62% for monohydrate and 38 to 44% for dihydrate (23). Also, the formation of 1st-CB_4 is more favorable than that of 1st-CB_3 because of the larger negative natural charge on the alcohol O-atom adjacent to the methyl group for TL (Fig. 4*A*).

The CBs are highly reactive because of an incomplete octet of electrons. Nucleophilic attack of 1st-CBs by DLs/TL yields additional CIs, which then undergo hydration and deprotonation to form the dimers (*SI Appendix*, Fig. S3). The natural bond orbitals (NBOs) of the MG-derived intermediates illustrate that the alcohol O-atom of DLs/TL exhibits a strongly negative natural charge, in contrast to the strongly positive natural charge center for CBs (Fig. 4*B*). Consequently, the electrostatic attraction between CBs and DLs/TL promotes the nucleophilic addition, representing the key feature for oligomerization (Fig. 5*A* and *SI Appendix*, Fig. S3 *A–D*). For 1st-CB_1 and 1st-CB_4, the cationic site with the adjacent methyl group is more positively charged, and the alcohol O···C distance at the cationic site is noticeably stretched with reduced steric hindrance. In contrast, steric hindrance is minimal for 1st-CB_2 and 1st-CB_3, while the cationic site without the adjacent methyl substituent is less positively charged. Subsequent protonation of the dimers followed by dehydration yields the second-generation carbenium ions, 2nd-CBs (*SI Appendix*, Fig. S4), which then engage in the association reactions with DLs/TL to form cyclic dimers or trimers (Fig. 5 *B* and *C* and *SI Appendix*, Fig. S5 *A–C*) and to propagate the oligomerization via multigenerational carbenium ions (M-CBs) (*SI Appendix*, Figs. S6 and S7). In this work, we consider only conformers with the lowest energies for larger oligomers (tetramers or higher) and the formation of six-membered ring oligomeric products, but as illustrated in *SI Appendix*, Fig. S8, the formation of five-membered ring oligomeric products is also possible (24).

For all pathways of the cationic oligomerization, we did not identify any TS. The barrierless nature of these reactions was further confirmed by scanning the pointwise potential curve (PPC) (*SI Appendix*, Fig. S9). Also, there exist competing reactions between CIs and hydroxide ions (OH^-) at each step of the oligomerization. Our calculations indicate that the competing reactions of the CIs (such as CI11, CI21, etc.) with OH^- are also barrierless (Fig. 1*B*), leading to an overall reversibility for oligomerization, i.e., CI11 + OH^- → MG + H_2O, CI31 + OH^- → DL + H_2O, etc. Hence, the fate of CIs at each step is determined

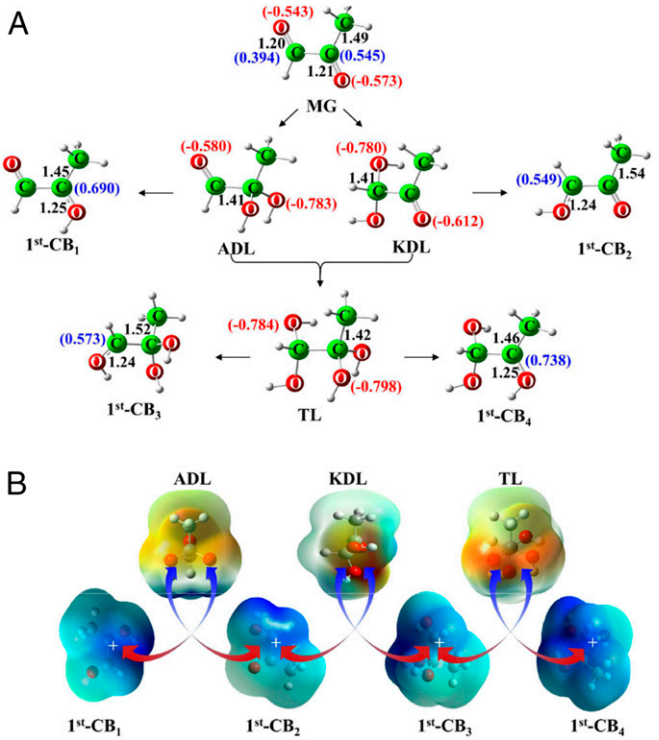

Fig. 4. The driving force for oligomerization. (*A*) Geometries of MG, DLs, TL, and 1st-CBs. The number in black denotes the bond length (in angstroms), and the numbers in blue and red label the positive and negative natural charges (in *e*), respectively. (*B*) The natural bond orbitals of DLs, TL, and CBs, with the blue and red colors depicting the maximum positive and negative charge densities, respectively. The arrow marks the nucleophilic attack of the positive charge center of CBs by the negatively charge alcohol group of DLs/TL, representing the key mechanism for oligomerization.

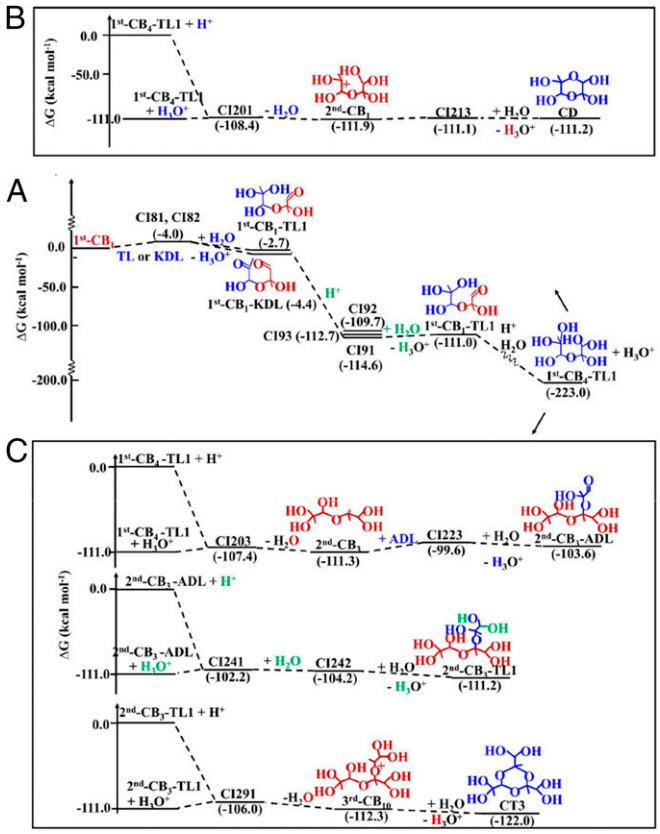

Fig. 5. Formation and propagation of oligomers. (*A*) PES starting from MG, 1st-CB_1, to 1st-CB_4-TL1 dimer. (*B*) PES starting from 1st-CB_4-TL1 to 2nd-CB_3-ADL, 2nd-CB_3-TL1, and CT3 trimers. (*C*) PES for intermolecular isomerization from 1st-CB_4-TL1 to cyclic dimer CD. The number in parentheses denotes the value of ΔG_r for each reaction step, and all energies are relative to MG. For comparison, MG protonation by the reaction with H_3O^+ is also shown in the figure.

by the competing reactions with OH^- for reversibility or hydration followed by further protonation for oligomerization. The forward process leading to oligomerization is dependent on pH and water activity; high acidity favors protonation but inhibits hydration because of reduced H_2O activity. On the other hand, the reverse process for the reactions of CIs with OH^- is dependent on pH and is unfavorable under acidic media (i.e., pH < 7). Our calculations indicate an intermediate range of pH for maximum oligomerization. Based on the quantum chemical calculations, we estimated the rate constants of (4.1–4.2) × 10^9 $M^{-1}\cdot s^{-1}$ for the aqueous reactions of MG (*SI Appendix*, Table S1), which are limited by liquid-phase diffusion. Our results indicate that the cationic mechanism is pH dependent, since protonation is favored in acidic solution but high acidity inhibits deprotonation and hydration due to decreased water activity (1). As a result, the cationic oligomerization only occurs efficiently in weakly acidic media, consistent with the previous experimental measurement showing an increasing Henry's Law constant and uptake coefficient of MG with decreasing acidity (16).

Furthermore, the carbenium ions bond readily with the basic nitrogen atom (with the prominent negative charge character) in ammonia/amines to form N-heterocycles (25, 26), responsible for rapid browning on ammonium/amine containing aerosols exposed to gaseous MG (19). In aqueous ammonium sulfate solution, NH_3 is in equilibrium with NH_4^+ (i.e., $NH_4^+ + H_2O \leftrightarrow NH_3 + H_3O^+$). Analogous to the cationic oligomerization, the nucleophilic addition to form N-heterocycles is promoted by the strong electrostatic attraction between CBs and NH_3 (*SI Appendix*, Fig. S10). Hence, the carbenium ion-mediated reactions involving ammonia/amines also represent a key pathway for BrC formation.

In contrast to previous speculation (16, 22), our results show kinetically and thermodynamically unfeasible hydration reactions of MG and unravel a mechanism of oligomer formation, including MG protonation followed by hydration and deprotonation to yield DLs and TL, protonation of DLs and TL followed by dehydration to form CBs, and formation and propagation of oligomers by nucleophilic addition of DLs/TL to CBs. Each of the steps is characterized by protonation with strong electrostatic attraction among the MG-derived intermediates, which are also enhanced by the methyl substituent effects. The cationic oligomerization is barrierless and occurs at fast rates in weakly acidic media characteristic of the tropospheric conditions (1, 27), i.e., on fine aerosols and cloud/fog droplets, to contribute to SOA and BrC formation from biogenic and anthropogenic emissions (1, 2, 6, 7). Our established mechanism is distinct from aldol condensation or acetal oligomerization previously investigated (22). The mechanism in this previous study involved initial hydration followed by H-migration and aldol condensation or nucleophilic attack for acetal oligomerization, both with high activation barriers of 20 to 30 $kcal\cdot mol^{-1}$. On the other hand, our protonation-initiated cationic oligomerization mechanism involves nucleophilic addition of diols/tetrol to carbenium ions, which is fast and barrierless.

A previous NMR study showed an exclusive KDL structure for aqueous MG solution. Our calculations showed that KDL is only a few kilocalories per mole more stable than ADL, similar to the theoretical work in ref. 22. Such a difference in their thermal stability is insufficient to explain KDL as the exclusive monohydrate form in MG solutions. On the other hand, our theoretical results indicated that the ADL pathway is more favorable kinetically, because of the larger NBO charge at the carbonyl site with the methyl substitution. Our results also showed that the proton affinity is higher for MG than for glyoxal. In addition, recent measurements showed that MG reacts more efficiently with base species (ammonia and amines) to form N-heterocycles than glyoxal, as evident by much a smaller single scattering albedo for the MG-base reactions on submicrometer particles. The reactions between α-carbonyls with ammonia/amines occur via an analogous nucleophilic addition, also indicative of a more favorable pathway for ADL (28).

Using the predicted liquid-phase rate constants, we estimated the aerosol growth rate by the aqueous reaction of MG under polluted conditions (*Methods*). Assuming 0.1-ppb concentration of MG and an aerosol mass concentration of 100 $\mu g\cdot m^{-3}$, a particle density of 1.6 $g\cdot cm^{-3}$, and a hydroscopic growth factor of 1.4, an aerosol growth rate of 4.4 $\mu g\cdot m^{-3}\cdot h^{-1}$ is derived, compared to that of about 10 $\mu g\cdot m^{-3}\cdot h^{-1}$ measured for rapid SOA growth during severe haze events in China (1, 2).

Conclusion

The carbenium ion-mediated reactions of small α-dicarbonyls occur efficiently on weakly acidic aerosols and cloud/fog droplets, contributing to SOA and BrC formation (1, 6, 7, 26, 29, 30). Atmospheric models without accounting for such a mechanism likely produce underestimation of the SOA and BrC budgets on urban, regional, and global scales and lead to uncertainty in assessing the aerosol direct and indirect radiative forcing on climate (5). Our work leaps ahead toward elucidating the fundamental chemical mechanisms of SOA and BrC formation and provides the key kinetics for incorporation of this pathway in atmospheric models to assess the aerosol impacts on air quality, human health, and climate. More broadly, we envisage that an insight into this aqueous chemistry has implications for diverse disciplines, from methylglyoxal metabolism of biological life to

organic synthesis and polymer materials (23, 31, 32). In particular, regulation of MG metabolism in microorganisms is of fundamental importance to biological life: Such a process involves detoxification of MG formed from a normal part of microbial metabolism by a set of enzymes (i.e., the glyoxalase system), with implications for aging, diabetes, and Alzheimer's disease as well as growth inhibition in different tumors (31, 32).

Methods

Although quantum chemical calculations have been extensively employed to investigate the gas-phase atmospheric chemistry (33, 34), fewer theoretical studies have been conducted to elucidate the atmospheric chemical mechanisms in the aqueous phase. In the present work, quantum chemical calculations were performed using the Gaussian 09 package (35). The solvent effect of water in the aqueous phase was considered by a continuum solvation model (SMD) (36, 37). The solvation free energy included two main components, including the bulk electrostatic contribution and cavity–dispersion–solvent-structure contribution from short-range interactions between the solute and solvent molecules (37). There were in total 112 aqueous ionic solvation free energies with 2,821 solvation data in the SMD model (37, 38), and the elements present in the solutes included charged atoms such as H, C, and O (37). Also, the previous study demonstrated that in evaluating the SMD model, an absolute aqueous solvation free energy of -265.9 kcal·mol^{-1} was used to treat proton stabilization by water (37), and this value was comparable to that of -264.0 kcal·mol^{-1} reported by Tissandier et al. (39). This method has been evaluated for over 112 ions in solution, including H^+ dissolving in water, and the errors has been identified to be less than 4 kcal·mol^{-1} (37). Geometry optimization of all stationary points (SPs), including the reactants, products, intermediates, and TSs, was performed by using density functional theory. The hybrid density functional M06-2X method was adopted with the 6-311G(d,p) basis set, i.e., at the M06-2X/6-311G(d,p) level (40). The thermodynamic contributions and harmonic vibrational frequencies were calculated at the same level as that for geometry optimization to identify all SPs as either the minima (zero imaginary frequency) or a TS (exactly with only one imaginary frequency). The minimum energy pathway was constructed with the intrinsic reaction coordinate theory to confirm that the TS accurately connected the reactants with the corresponding products. TS was searched by examining the SP using the TS keyword in geometry optimization, while the absence of a TS was confirmed if no energy exceeded the bond dissociation energy along the reaction coordinate (41–44). In addition, the PPC scanning was performed to confirm a barrierless process at the M06-2X/6-311G(d,p) level (45). For this method, except for fixing the internal breaking or forming bond length, all other geometric parameters were fully optimized. An example of the calculated PPC (for the R_H+11 pathway in *SI Appendix*, Fig. S9) shows the relative energy (E_{rel}) regarding the reactants (MG and H^+). The forming O–H bond was successively varied from 0.8 to 4.8 Å with an interval of 0.1 Å, while other geometric parameters were fully optimized for the given O–H value. The minimum energy occurs at the O–H distance of 1.0 Å, corresponding to the product CI11, and the energy increases successively as the O–H distance increases. The energy is nearly constant at the O–H distance of about 3.0 Å and approaches asymptotically to those of the reactants. Hence, the maximum energy point corresponds to the reactants MG and H^+, rather than a transition state, confirming that the protonation reaction represents a barrierless process.

The dual-level potential profile along the reaction path was further refined with a more flexible basis set 6-311 + G(3df,3pd), i.e., at the M06-2X/6-311 + G(3df,3pd) level. The dual-level approach was denoted as X//Y, where a single-point energy calculation at level X was carried out for the geometry optimized at a lower level Y. Energetic calculations employing the CCSD(T)/6-311 + G(2df,2p) level, i.e., coupled cluster approach with single and double substitutions including a perturbative estimate of connected triples substitutions with the flexible 6-311 + G(2df,2p) basis set, were also performed to justify the performance of the M06-2X method for describing the PES. To further evaluate the results at the M06-2X//M06-2X level, higher-level calculations using the CCSD(T)/6-311 + G(2df,2p) level were performed to refine the energetics for the reaction pathways of R1 (*SI Appendix*, Table S2). For example, the $\Delta G^{\ddagger}$ value of 44.1 kcal·mol^{-1} for TS1 at the M06-2X//M06-2X level is only slightly lower than that at the CCSD(T)//M06-2X level (47.1 kcal·mol^{-1}). The difference in the ΔG_r values between the two methods is within 2.5 kcal·mol^{-1} for the reaction pathways of R1, indicating that the M06-2X//M06-2X level provides reliable energetic descriptions of the MG oligomerization. The structural parameters of all possible ionic reaction pathways are summarized in *SI Appendix*, Table S3. Based on the above PES information, the reaction kinetics were calculated using conventional TST, solvent cage effects (36), and diffusion-limited effects (29), as shown in *SI Appendix*.

Data Availability. All data relevant to this research are available in the main text and *SI Appendix*.

ACKNOWLEDGMENTS. This work was supported by National Natural Science Foundation of China Grants (41731279 and 41675122); Local Innovative and Research Teams Project of Guangdong Pearl River Talents Program (2017BT01Z032); Natural Science Foundation of Guangdong Province, China (2019B151502064); Science and Technology Program of Guangzhou City (201707010188); a collaborative research program between Texas A&M University and the National Natural Science Foundation of China; Innovation Team Project of Guangdong Provincial Department of Education (2017KCXTD012); Science and Technology Key Project of Guangdong Province, China (2019B110206002); and the Robert A. Welch Foundation Grant (A-1417). Additional support for this research was provided by the Texas A&M University Supercomputing Facilities. We acknowledge the use of the Laboratory for Molecular Simulations at Texas A&M University. A.L.Z. was supported by a fellowship from the Robert A. Welch Foundation.

1. R. Zhang *et al.*, Formation of urban fine particulate matter. *Chem. Rev.* **115**, 3803–3855 (2015).
2. K. A. Rychlik *et al.*, In utero ultrafine particulate matter exposure causes offspring pulmonary immunosuppression. *Proc. Natl. Acad. Sci. U.S.A.* **116**, 3443–3448 (2019).
3. G. Wu *et al.*, Adverse organogenesis and predisposed long-term metabolic syndrome from prenatal exposure to fine particulate matter. *Proc. Natl. Acad. Sci. U.S.A.* **116**, 11590–11595 (2019).
4. World Health Organization, Air pollution, Geneva, Switzerland (2018). https://www.who.int/health-topics/air-pollution#tab=tab_1 Accessed 19 May 2020.
5. Intergovernmental Panel on Climate Change, *Climate Change 2013: The Physical Science Basis. Contribution of Working Group I to the Fifth Assessment Report of the Intergovernmental Panel on Climate Change*, (Cambridge University Press, 2013).
6. Z. An *et al.*, Severe haze in northern China: A synergy of anthropogenic emissions and atmospheric processes. *Proc. Natl. Acad. Sci. U.S.A.* **116**, 8657–8666 (2019).
7. M. Shrivastava *et al.*, Recent advances in understanding secondary organic aerosol: Implications for global climate forcing. *Rev. Geophys.* **55**, 509–559 (2017).
8. C. L. Heald *et al.*, A large organic aerosol source in the free troposphere missing from current models. *Geophys. Res. Lett.* **32**, 109–127 (2005).
9. Y. B. Lim *et al.*, Aqueous chemistry and its role in secondary organic aerosol (SOA) formation. *Atmos. Chem. Phys.* **10**, 10521–10539 (2010).
10. S. Guo *et al.*, Elucidating severe urban haze formation in China. *Proc. Natl. Acad. Sci. U.S.A.* **111**, 17373–17378 (2014).
11. J. Fan *et al.*, Effects of aerosol optical properties on deep convective clouds and radiative forcing. *J. Geophys. Res.* **113**, D08209 (2008).
12. Y. Wang *et al.*, Assessing the effects of anthropogenic aerosols on Pacific storm track using a multiscale global climate model. *Proc. Natl. Acad. Sci. U.S.A.* **111**, 6894–6899 (2014).
13. T. M. Fu *et al.*, Global budgets of atmospheric glyoxal and methylglyoxal, and implications for formation of secondary organic aerosols. *J. Geophys. Res.* **113**, D15303 (2008).
14. Y. Ji *et al.*, OH-initiated oxidation of acetylacetone: Implications for ozone and secondary organic aerosol formation. *Environ. Sci. Technol.* **52**, 11169–11177 (2018).
15. M. Kalberer *et al.*, Identification of polymers as major components of atmospheric organic aerosols. *Science* **303**, 1659–1662 (2004).
16. J. Zhao, N. P. Levitt, R. Zhang, J. Chen, Heterogeneous reactions of methylglyoxal in acidic media: Implications for secondary organic aerosol formation. *Environ. Sci. Technol.* **40**, 7682–7687 (2006).
17. M. E. Gomez, Y. Lin, S. Guo, R. Zhang, Heterogeneous chemistry of glyoxal on acidic solutions. An oligomerization pathway for secondary organic aerosol formation. *J. Phys. Chem. A* **119**, 4457–4463 (2015).
18. J. H. Kroll *et al.*, Chamber studies of secondary organic aerosol growth by reactive uptake of simple carbonyl compounds. *J. Geophys. Res.* **110**, D23207 (2005).
19. D. O. De Haan *et al.*, Brown carbon production in ammonium- or amine-containing aerosol particles by reactive uptake of methylglyoxal and photolytic cloud cycling. *Environ. Sci. Technol.* **51**, 7458–7466 (2017).
20. L. Wang *et al.*, Laboratory investigation on the role of organics in atmospheric nanoparticle growth. *J. Phys. Chem. A* **115**, 8940–8947 (2011).
21. D. O. De Haan *et al.*, Nitrogen-containing, light-absorbing oligomers produced in aerosol particles exposed to methylglyoxal, photolysis, and cloud cycling. *Environ. Sci. Technol.* **52**, 4061–4071 (2018).
22. H. E. Krizner, D. O. De Haan, J. Kua, Thermodynamics and kinetics of methylglyoxal dimer formation: A computational study. *J. Phys. Chem. A* **113**, 6994–7001 (2009).
23. I. Nemet, D. Vikić-Topić, L. Varga-Defterdarović, Spectroscopic studies of methylglyoxal in water and dimethylsulfoxide. *Bioorg. Chem.* **32**, 560–570 (2004).
24. N. Sedehi *et al.*, Temperature- and pH-dependent aqueous-phase kinetics of thereactions of glyoxal and methylglyoxal with atmospheric amines andammonium sulfate. *Atmos. Environ.* **77**, 656–663 (2013).
25. T. Moise, J. M. Flores, Y. Rudich, Optical properties of secondary organic aerosols and their changes by chemical processes. *Chem. Rev.* **115**, 4400–4439 (2015).

26. J. Kua, H. E. Krizner, D. O. De Haan, Thermodynamics and kinetics of imidazole formation from glyoxal, methylamine, and formaldehyde: A computational study. *J. Phys. Chem. A* **115**, 1667–1675 (2011).
27. G. Wang *et al*., Persistent sulfate formation from London Fog to Chinese haze. *Proc. Natl. Acad. Sci. U.S.A.* **113**, 13630–13635 (2016).
28. W. Marrero-Ortiz *et al*., Formation and optical properties of brown carbon from small α-dicarbonyls and amines. *Environ. Sci. Technol.* **53**, 117–126 (2019).
29. F. Zhang *et al*., An unexpected catalyst dominates formation and radiative forcing of regional haze. *Proc. Natl. Acad. Sci. U.S.A.* **117**, 3960–3966 (2020).
30. Y. Wang, A. Khalizov, M. Levy, R. Y. Zhang, New Directions: Light absorbing aerosols and their atmospheric impacts. *Atmos. Environ.* **81**, 713–715 (2013).
31. P. J. Thornalley, The glyoxalase system: New developments towards functional characterization of a metabolic pathway fundamental to biological life. *Biochem. J.* **269**, 1–11 (1990).
32. P. Matafome, T. Rodrigues, C. Sena, R. Seiça, Methylglyoxal in metabolic disorders: Facts, myths, and promises. *Med. Res. Rev.* **37**, 368–403 (2017).
33. R. Zhang *et al*., Atmospheric new particle formation enhanced by organic acids. *Science* **304**, 1487–1490 (2004).
34. K. T. Kuwata *et al*., Quantum chemical and statistical rate theory studies of the vinyl hydroperoxides formed in trans-2-butene and 2,3-dimethyl-2-butene ozonolysis. *J. Phys. Chem. A* **122**, 2485–2502 (2018).
35. M. Frisch *et al*., Gaussian 09 (Gaussian, Inc., Wallingford, CT, 2009).
36. Y. Gao, Y. Ji, G. Li, B. Mai, T. An, Bioaccumulation and ecotoxicity increase during indirect photochemical transformation of polycyclic musk tonalide: A modeling study. *Water Res.* **105**, 47–55 (2016).
37. A. V. Marenich, C. J. Cramer, D. G. Truhlar, Universal solvation model based on solute electron density and on a continuum model of the solvent defined by the bulk dielectric constant and atomic surface tensions. *J. Phys. Chem. B* **113**, 6378–6396 (2009).
38. V. S. Bernales, A. V. Marenich, R. Contreras, C. J. Cramer, D. G. Truhlar, Quantum mechanical continuum solvation models for ionic liquids. *J. Phys. Chem. B* **116**, 9122–9129 (2012).
39. M. D. Tissandier *et al*., The proton's absolute aqueous enthalpy and Gibbs free energy of solvation from cluster-ion solvation data. *J. Phys. Chem. A* **102**, 7787–7794 (1998).
40. Y. Ji *et al*., Reassessing the atmospheric oxidation mechanism of toluene. *Proc. Natl. Acad. Sci. U.S.A.* **114**, 8169–8174 (2017).
41. D. Zhang, R. Zhang, Ozonolysis mechanisms of alpha-pienes and beta-pienes: Kinetics and mechanism. *J. Chem. Phys.* **122**, 114308 (2005).
42. I. Suh, W. F. Lei, R. Y. Zhang, Experimental and theoretical studies of isoprene reaction with NO_3. *J. Phys. Chem.* **105**, 6471–6478 (2001).
43. W. F. Lei, A. Derecskei-Kovacs, R. Y. Zhang, Ab initio study of OH addition reaction to isoprene. *J. Chem. Phys.* **113**, 5354–5360 (2000).
44. J. Zhao, R. Zhang, E. C. Fortner, S. W. North, Quantification of hydroxycarbonyls from OH-isoprene reactions. *J. Am. Chem. Soc.* **126**, 2686–2687 (2004).
45. M. K. Hazra, A. Sinha, Formic acid catalyzed hydrolysis of SO_3 in the gas phase: A barrierless mechanism for sulfuric acid production of potential atmospheric importance. *J. Am. Chem. Soc.* **133**, 17444–17453 (2011).